Astronomy & Astrophysics

The ionizing photon production efficiency of star-forming galaxies at *z* ∼ 4–10

M. Llerena[1],[*][iD], L. Pentericci[1], L. Napolitano[1,2][iD], S. Mascia[1,3][iD], R. Amorín[4][iD], A. Calabrò[1], M. Castellano[1],
N. J. Cleri[5,6,7], M. Giavalisco[8][iD], N. A. Grogin[9][iD], N. P. Hathi[9], M. Hirschmann[10][iD], A. M. Koekemoer[9][iD],
T. Nanayakkara[11][iD], F. Pacucci[12,13][iD], L. Shen[14], S. M. Wilkins[15,16][iD], I. Yoon[17][iD], L. Y. A. Yung[9][iD],
R. Bhatawdekar[18], R. A. Lucas[9][iD], X. Wang[19,20,21], P. Arrabal Haro[22],[**][iD], M. B. Bagley[23][iD], S. L. Finkelstein[23],
J. S. Kartaltepe[24], E. Merlin[1][iD], C. Papovich[14,25], N. Pirzkal[26], and P. Santini[1][iD]

(Affiliations can be found after the references)

ABSTRACT

Context. Investigating the ionizing emission of star-forming galaxies and the escape fraction of ionizing photons is critical to understanding their contribution to reionization and their impact on the surrounding environment. The number of ionizing photons available to reionize the intergalactic medium (IGM) depends on not only the abundance of galaxies but also their efficiency in producing ionizing photons (ξ_{ion}). This quantity is thus fundamental to quantify the role of faint versus bright sources in driving this process, as we must assess their relative contribution to the total ionizing emissivity.

Aims. Our goal is to estimate the ξ_{ion} using Balmer lines (Hα or Hβ) in a sample of 761 galaxies at $4 \leq z \leq 10$ selected from different JWST spectroscopic surveys. We aim to determine the redshift evolution of ξ_{ion} and the relation of ξ_{ion} with the physical properties of the galaxies.

Methods. We used the available HST and JWST photometry to perform a spectral energy distribution (SED) fitting in the sample to determine their physical properties and relate them with ξ_{ion}. We used the BAGPIPES code for the SED fitting and assumed a delayed exponential model for the star formation history. We used the NIRSpec spectra from prism or grating configurations to estimate Balmer luminosities, and then constrained ξ_{ion} values after dust correction.

Results. We find a mean value of $10^{25.22}$ Hz erg^{-1} for ξ_{ion} in the sample with an observed scatter of 0.42 dex. We find an increase in the median values of ξ_{ion} with redshift from $10^{25.09}$ Hz erg^{-1} at $z \sim 4.18$ to $10^{25.28}$ Hz erg^{-1} at $z \sim 7.14$, confirming the redshift evolution of ξ_{ion} found in other studies. Regarding the relation between ξ_{ion} and physical properties, we find a decrease in ξ_{ion} with increasing stellar mass, indicating that low-mass galaxies are efficient producers of ionizing photons. We also find an increase in ξ_{ion} with increasing specific star formation rate (sSFR) and increasing UV absolute magnitude. This indicates that faint galaxies and galaxies with high sSFR are also efficient producers. We also investigated the relation of ξ_{ion} with the rest-frame equivalent width (EW) of [OIII]λ5007 and find that galaxies with the higher EW([OIII]λ5007) are more efficient producers of ionizing photons, with the best fit leading to the relation $\log(\xi_{ion}) = 0.43 \times \log(EW[OIII]) + 23.99$. Similarly, we find that galaxies with higher O32 = [OIII]λ5007/[OII]$\lambda\lambda$3727,3729 and lower gas-phase metallicities (based on the R23 = ([OIII]$\lambda\lambda$4959,5007+[OII]$\lambda\lambda$3727,3729)/Hβ calibration) show higher ξ_{ion} values.

Key words. galaxies: evolution – galaxies: formation – galaxies: high-redshift – galaxies: ISM – galaxies: starburst

1. Introduction

The epoch of reionization (EoR) marks a critical phase in the evolution of the Universe, during which the intergalactic medium (IGM) became transparent to Lyman continuum (LyC) radiation (energy ≥13.6 eV). Observations suggest that this epoch concluded around redshift $z \sim 6$ (Fan et al. 2006; Yang et al. 2020), though some research indicates reionization may have extended closer to $z \sim 5$ (Bosman et al. 2022). The consensus is that young, massive stars within galaxies played a major role in this transformation by producing large quantities of LyC photons, which escaped from the interstellar medium (ISM) and ultimately ionized the IGM (e.g., Rosdahl et al. 2018). However, debate persists over whether faint, low-mass galaxies and bright, massive galaxies, or a combination of the two contributed the most to the reionization photon budget (Finkelstein et al. 2019; Naidu et al. 2020; Robertson 2022). Additionally, the role of active galactic nuclei (AGNs) in reionization may be more sig-

nificant than previously thought, with some studies suggesting that AGNs and their host galaxies account for over 10% of the photon budget (Maiolino et al. 2024; Madau et al. 2024).

Investigating the ionizing emission of star-forming galaxies is critical to understanding their contribution to reionization and their impact on the surrounding environment. The number of ionizing photons available to reionize the IGM depends on not only the abundance of galaxies but also their efficiency in producing LyC radiation and the fraction of this radiation, which escapes into the IGM. This quantity is thus fundamental to quantify the role of faint versus bright sources in driving this process, as we must assess their relative contribution to the total ionizing emissivity ($\dot{n}_{ion}$) – the number of ionizing photons emitted per unit time and commoving volume. This is commonly expressed as

$$\dot{n}_{ion} = \rho_{UV}\xi_{ion}f_{esc}, \tag{1}$$

where ρ_{UV} is the commoving total UV luminosity density (erg s^{-1} Hz^{-1} Mpc^{-3}), f_{esc} is the fraction of LyC photons that escape from galaxies to ionize intergalactic hydrogen, and ξ_{ion}

is the ionizing photon production efficiency ($Hz\,erg^{-1}$), which indicates the number of LyC photons per unit UV luminosity density by the stellar populations in galaxies. The quantity, $\dot{n}_{ion}$, represents the commoving density of LyC photons produced per unit time available for ionizing hydrogen in the IGM. Each of these three components carries significant uncertainties in both modeling and observation, making it extremely difficult to model them consistently. This challenge arises because the underlying physical processes span many orders of magnitude in scale.

For galaxies to be the primary drivers of reionization, relatively high escape fractions of ionizing photons are required, typically ranging from 10% to 20% (Robertson et al. 2013; Finkelstein et al. 2019; Naidu et al. 2020; Yung et al. 2020a). Another crucial factor is the ξ_{ion}. Standard reionization models (e.g., Madau et al. 1999; Robertson et al. 2013) find a value of $\log\xi_{ion}[Hz\,erg^{-1}] = 25.2$–$25.3$ for star-forming galaxies, which is in agreement with observations at $z \sim 4$ (e.g., Bouwens et al. 2016). Throughout the paper, we consider a value of $\log\xi_{ion}[Hz\,erg^{-1}] = 25.27$ as the canonical value based on observations. Recent observations, which extend up to redshift $z \sim 9$, show that ξ_{ion} increases at higher redshifts (Tang et al. 2023; Simmonds et al. 2024; Pahl et al. 2025; Atek et al. 2024; Begley et al. 2025). This rise in ξ_{ion} implies that lower escape fractions are needed for galaxies to have been the main contributors to reionization.

The launch of the *James Webb* Space Telescope (JWST; Gardner et al. 2006, 2023) has provided unprecedented access to the rest-frame optical range at high redshifts, offering valuable new data to improve our understanding of ξ_{ion} and its variation across galaxy populations. As a result, studies focusing on how f_{esc} and ξ_{ion} evolve with galaxy properties, especially at high redshifts, are critical for advancing our understanding of the EoR. A key observation is that stellar mass correlates with its ability to produce ionizing photons (Castellano et al. 2023).

A detailed and thorough study of ξ_{ion} requires large and representative samples with spectroscopic Hα and Hβ observations to measure nebular line luminosity directly and properly correct for dust. One method of measuring ξ_{ion} that would enable us to constrain its value for individual galaxies is to use nebular recombination lines (e.g., Hα). In an ionization-bounded nebula, the recombination rate balances the rate of photons with energies at or above 13.6 eV that are either emitted by the star or produced during recombination to the hydrogen ground level.

In this paper, we present a sample of 761 spectroscopically confirmed galaxies with NIRSpec (Jakobsen et al. 2022) at $4 \leq z \leq 10$ from different JWST programs to estimate their individual ξ_{ion} values based on Balmer lines. We also estimated their physical properties based on fitting their spectral energy distribution (SED) using the available NIRCam (Beichman et al. 2012) photometry of these sources. This paper is organized as follows: In Sect. 2 we describe the sample selection. In Sect. 3 we describe the data analysis, which includes emission line measurements, SED fitting, UV luminosity estimations, and ξ_{ion} calculations for individual galaxies. In Sect. 4.1 we discuss the evolution of ξ_{ion} with redshift. In Sect. 4.2 we show the relation between ξ_{ion} and UV absolute magnitude (M_{UV}), as well as the evolution with redshift. In Sect. 4.3 we analyze the total ionizing emissivity using the relation found in this paper. In Sect. 4.4 we show the dependency of ξ_{ion} on the physical properties, which include stellar mass and specific star formation rate (sSFR). In Sect. 4.5 we show the relation of ξ_{ion} with the rest-frame equivalent width (EW) of [OIII]$\lambda5007$. In Sect. 4.6 we discuss the relation of ξ_{ion} with line flux ratios and gas-phase metallicity. Lastly, we present our summary and conclusions in Sect. 5.

Throughout this paper, we adopt a Λ-dominated flat universe with $\Omega_\Lambda = 0.7$, $\Omega_M = 0.3$, and $H_0 = 70\,km\,s^{-1}\,Mpc^{-1}$. All magnitudes are quoted in the AB system (Oke & Gunn 1983). Equivalent widths are quoted in the rest frame and are positive for emission lines. We consider $\log(O/H)_\odot = 8.69$ (Asplund et al. 2009).

2. Data and sample selection

We selected galaxies at redshift $z = 4$–10 in order to include the rest-UV and Hβ in the prism configuration using NIRSpec. We selected galaxies from the cosmic evolution early release science survey (CEERS; Finkelstein et al. 2023), the JWST advanced deep extragalactic survey (JADES; Eisenstein et al. 2023), the GLASS survey (Treu et al. 2022), and the program GO-3073 (PI: M. Castellano). We describe the selection in each survey in the next subsections. Our final sample includes 790 galaxies.

2.1. The CEERS survey

The complete CEERS program involved imaging with the NIRCam short and long-wavelength channels in ten pointings, observed as coordinated parallels to primary observations with the NIRSpec and the midinfrared instrument (MIRI; Wright et al. 2015). In this paper, we used photometric data from NIRCam and NIRSpec spectra. In total, ten pointings were taken with NIRCam imaging, including seven filters per pointing (F115W, F150W, F200W, F277W, F356W, F410M, and F444W).

We used version v0.51.2 of the CEERS Photometric Catalogs (Finkelstein et al. in prep). The catalog contains 101808 sources. The NIRCam images used are publicly available, and we refer the reader to Bagley et al. (2023) for a complete description of the data reduction. For the pointings 1, 2, 3, and 6, the images are available in the Data Release 0.5[1], while for the pointings 4, 5, 7, 8, 9, and 10, the images are available in the Data Release 0.6[2].

A complete description of the photometric catalog will be presented in Finkelstein et al. in prep. Briefly, the photometry was performed with SExtractor (v2.25.0; Bertin & Arnouts 1996) with F277W and F356W as the detection image. The fiducial fluxes were measured in small Kron apertures corrected by large-scale flux, following the methodology in Finkelstein et al. (2023). This photometry also makes use of archival HST data on this field from programs including CANDELS (Koekemoer et al. 2011; Grogin et al. 2011).

The CEERS survey also includes six NIRSpec pointings, numbered p4, p5, p7, p8, p9, and p10. Each of these pointings has observations with the three NIRSpec medium resolution (MR) gratings (G140M, G235M, and G395M) and with the low-resolution Prism. Two more fields, p11 and p12, were observed with the prism in February 2023 because the prism observations p9 and p10 were severely impacted by a short circuit. The grating set covers from 0.97–5.10 μm with a resolving power $R = \lambda/\Delta\lambda$ of ~1000, while the prism covers from 0.60–5.30 μm with a resolving power of $30 < R < 300$, depending on the wavelength.

We adopted the NIRSpec data produced by the CEERS collaboration using the STScI JWST Calibration Pipeline[3] (Bushouse et al. 2022). Specifically, we used the JWST pipeline

---

[1] https://ceers.github.io/dr05.html
[2] https://ceers.github.io/dr06.html
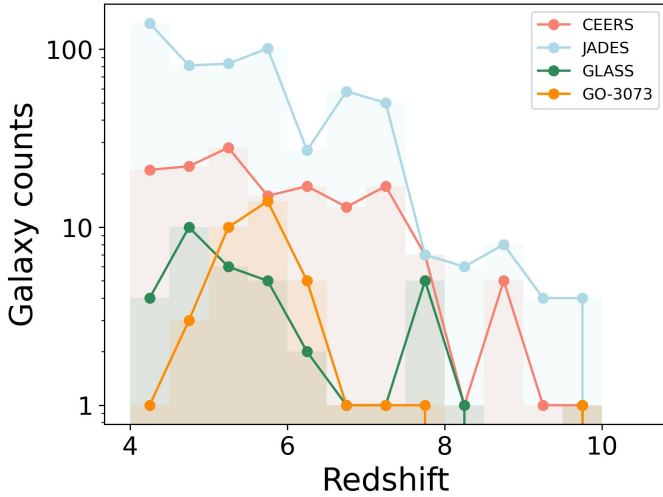[3] https://github.com/spacetelescope/jwst

Fig. 1. Redshift distribution of the selected sample of spectroscopically confirmed galaxies at $4 \leq z \leq 10$ in the different surveys considered in this work, as described in the main text.

to perform standard reductions, including the removal of dark current and bias, flat-fielding, background, photometry, wavelength, and slit loss correction for each exposure. We also performed additional reductions to remove the $1/f$ noise and the snowballs. The 2D spectra of each target were then rectified and combined to generate the final 2D spectra. The details of the data reduction are presented in Arrabal Haro et al. (2023) and Arrabal Haro et al. in prep.

We selected galaxies with NIRSpec spectra at redshifts $4 \leq z \leq 10$. We adopt a lower redshift limit of $z = 4$ to ensure that the ~1200 Å range is observed in the prism configuration, and a higher redshift limit of $z = 10$ to ensure that Hβ is observed. We did not consider NIRSpec data observed in pointings 9 and 10, since, due to a short circuit issue, they are contaminated and lack secure flux calibrations. We selected galaxies with available NIRCam photometry. Our sample consists of 148 galaxies, 140 with prism observations and 32 with MR grating observations. The redshift distribution of the sample is shown in red in Fig. 1.

2.2. The JADES survey

We considered the third public data release of the survey (D'Eugenio et al. 2025) to select our sample. JADES provides both imaging and spectroscopy in the two GOODS fields. Spectroscopy consists of medium-depth and deep NIRSpec/MSA spectra of 4000 targets, covering the spectral range 0.6–5.3 µm and observed with both the low-dispersion prism ($R = 30$–300) and the three medium-resolution gratings ($R = 500$–1500). We refer to (D'Eugenio et al. 2025) for a complete description of observations, data reduction, sample selection, and target allocation. A total of 2053 redshifts were measured from multiple emission lines in this data release. The photometric catalog includes observation using the NIRCam wide-broad filters F090W, F115W, F150W, F200W, F277W, F356W, F444W, and the medium-broad filters F182M, F210M, F335M, F410M, F430M, F460M, F480M.

We selected galaxies with NIRSpec spectra at redshift $4 \leq z \leq 10$. We selected galaxies with NIRCam photometry. Our sample thus includes 314 galaxies (240 with MR and 314 with prism) in the GOODS-South field and 255 galaxies (239 with MR and 246 with prism) in the GOODS-North field. The red-

shift distribution of the total sample of 569 galaxies is shown in lightblue in Fig. 1.

2.3. The GLASS survey

The GLASS survey obtained deep observations of galaxies in the Hubble Frontier Field cluster, Abell 2744, with both NIRCam photometry and NIRSpec spectroscopy. The public catalog includes galaxies observed with prism and the high-resolution (HR) G140H, G235H, and G395H grating. The public spectroscopic data release is found in Mascia et al. (2024b). We use the NIRSpec data reduced by the Cosmic Dawn Center, which is published on the DAWN JWST Archive (DJA)[4]. The photometric catalog includes observations using the NIRCam wide-broad filters F115W, F150W, F200W, F277W, F356W, F444W, and the medium-broad filters F410M (Merlin et al. 2024).

We selected galaxies with NIRSpec spectra at redshift $4 \leq z \leq 10$ and with NIRCam photometry. Our sample includes 36 galaxies (23 with HR and 25 with prism) and its redshift distribution is shown in green in Fig. 1.

2.4. The GO-3073 program

The program observed the cluster Abell-2744 using the prism configuration of NIRSpec. In this study, we considered data obtained during the first epoch (October 24, 2023), divided into three visits, each with an exposure time of 6567 s. Unfortunately, an electrical short affected the third visit, so we excluded it from the final reduction. The data were processed using version 1.13.4 of the STScI Calibration Pipeline, with calibration reference data system (CRDS) mapping 1197. Further details on observations and data reduction are provided in Napolitano et al. (2025). The photometric catalog includes observations using the NIRCam wide-broad filters F090W, F115W, F150W, F200W, F277W, F356W, F444W (Merlin et al. 2024).

We selected 37 galaxies with $4 < z < 10$ with NIRSpec, NIRCam photometry, and secure spectroscopic redshift. The redshift distribution of the sample is shown in orange in Fig. 1.

3. Data analysis

3.1. AGN removal and complete subsample

We first removed AGNs from our final sample based on the AGN sources identified in Roberts-Borsani et al. (2024) and Brooks et al. (2024). Their selection criteria for AGNs is based on broad + narrow component models to reproduce the Hα profiles, while the [OIII]λ5007 profile is reproduced by a single narrow component. Following this criterion, we removed 12 sources from the CEERS survey, 14 sources from the JADES survey, 1 source from the GLASS survey, and 2 sources from the GO-3073 program. Therefore, in the following sections, we consider a final sample of 761 galaxies. We note that our sample might still be contaminated by narrow obscured AGNs, but there is no clear method to select them at high z. We discuss this possible contamination in Appendix A.

We selected a subsample based on the detection limits of the surveys. We called this subsample the complete sample. We assumed a 5σ depth of 29.3 mag in F200W for a point source in the CEERS survey (Finkelstein et al. 2025), which is the shal-

---

[4] `https://dawn-cph.github.io/dja/spectroscopy/nirspec/`
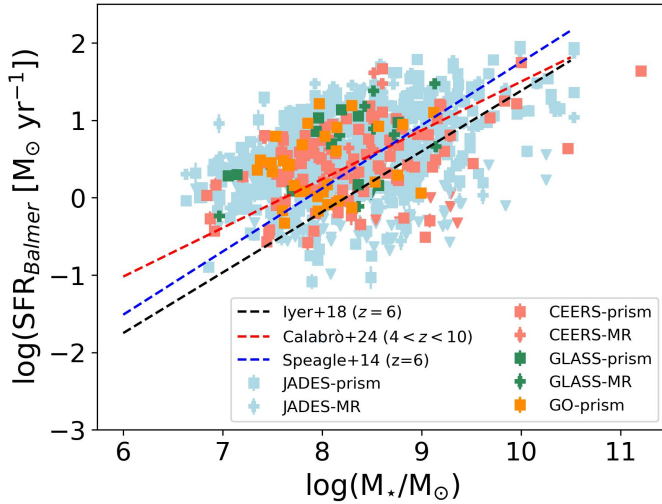
Fig. 2. Distribution of the full sample along the stellar mass-SFR plane. The dashed black and blue lines are the main-sequence of star-forming galaxies at $z = 6$ from Iyer et al. (2018) and Speagle et al. (2014), respectively. While the dashed red line represents the main-sequence at $4 < z < 10$ from Calabrò et al. (2024b). The triangle symbols are upper limits based on $H\alpha$ or on $H\beta$ if an upper limit on $H\alpha$ is not estimated.

lowest survey we considered. The complete sample includes 570 galaxies above those depths.

3.2. Emission line measurements

To measure ξ_{ion} in individual galaxies, we needed to estimate the luminosity of Balmer lines. In this case, we considered $H\alpha$ and $H\beta$ lines. For part of the analysis in the following sections, we also considered [OIII]$\lambda 5007$ and the unresolved doublet [OII]$\lambda 3729$ in the set of lines to measure.

For the CEERS survey, we considered the measurements included in the data release 0.9 (Arrabal Haro et al. in prep.). The set of measurements was performed using LiMe[5] (Fernández et al. 2024), which is a library that provides a set of tools to fit the lines in astronomical spectra.

For consistency, we used the same code to measure the line for the sample in the other surveys. We considered one Gaussian to model the line profiles. For the galaxies in the GLASS survey and the GO-3073 program, we corrected the fluxes for magnification using the lens model presented in Bergamini et al. (2023). We also checked the flux calibration of the spectra based on the available photometry, and we corrected the observed fluxes by a factor of ~30% of flux losses based on the median value in all the photometric bands. This correction does not depend sensibly on the wavelength, in agreement with what was found by Roberts-Borsani et al. (2024).

We corrected the line fluxes for dust reddening using the Calzetti et al. (2000) attenuation law. We considered the $E(B-V)$ value derived from the SED fitting for galaxies, as described in the following Sect. 3.3. As a caveat, we did not consider the Balmer decrement in this project in order to have a homogeneous dust correction for all galaxies in the sample. When comparing $E(B-V)$ values from Balmer lines and SED fitting, we find a difference by a factor of 0.47 (median) and 1.53 (mean). To avoid artificial trends induced by using different methods to estimate $E(B-V)$ for the whole sample, we opted to consider the

---

[5] https://lime-stable.readthedocs.io/en/latest/

values from the SED fitting for dust attenuation. As we show in Sect. 3.5 and Appendix B, we find good agreement between the luminosities of $H\alpha$ and $H\beta$, which corroborates the robustness of our dust correction.

3.3. SED fitting

We used BAGPIPES (Carnall et al. 2018) version 1.2.0 to estimate the physical parameters with the Bruzual & Charlot (2003) stellar population models. We fixed the redshift to the spectroscopic redshift. We considered a delayed exponential τ-model for the star formation history (SFH), where τ is the timescale of the decrease in the SFH. In the model, we consider an age ranging from 1 Myr to the age of the Universe at the observed redshift. We allowed the τ parameter to vary between 0.1 and 10 Gyr, and the metallicity to vary freely up to $0.5\,Z_\odot$. The upper limit in stellar metallicity is based on the stellar mass-metallicity relation observed at $z = 3.5$ for a stellar mass of $10^{11}\,M_\odot$ (Llerena et al. 2022; Stanton et al. 2024). For the dust component, we considered the Calzetti et al. (2000) attenuation curve and let the A_V parameter vary between $0-2$ mag. We also included a nebular component in the model, and we let the ionization parameter freely vary between -4 and 0. We used the same recipe for all the galaxies in all surveys using the available photometry. The observed photometry of galaxies in the GLASS survey and in the GO-3073 program is corrected using the same lensing model available in Bergamini et al. (2023).

We also converted the dust-corrected $L(H\alpha)$ to SFR assuming the calibration from Reddy et al. (2022) as SFR(Balmer) = $L(H\alpha) \times 10^{-41.67}$. This is the most suited calibration according to the typical subsolar metallicities expected for our galaxies at $z > 4$, and reflects the greater efficiency of ionizing photon production in metal-poor stellar populations. The distribution of the sample along the main sequence at $z = 6$ (Iyer et al. 2018; Speagle et al. 2014) is displayed in Fig. 2. As a reference, we also show the main sequence from Calabrò et al. (2024b) that includes a wide range of redshifts between $z = 4$ and $z = 10$. Our sample is scattered around the main sequence, and the galaxies cover ~3 dex in stellar mass and SFR. We note that there is no bias in stellar mass or SFR between the various subsamples depending on the considered survey. Nonetheless, less massive sources with $M_* \lesssim 10^{7.5}\,M_\odot$ tend to be above the main sequence, independently of the relation we use as reference.

3.4. UV luminosity density

We determined the UV luminosity density by estimating the value of the rest-frame continuum at 1500 Å based on the SED model. For this purpose, we considered a synthetic top-hat filter of bandwidth 100 Å centered at 1500 Å to convolve with the SED model. Additionally, we followed Pahl et al. (2025) and estimated the uncertainty of the UV luminosity density by considering the mean uncertainty of the flux density in the observed filters covering the rest-frame from 1200 to 3000 Å. In this way, the error bars are motivated by nearby photometric constraints. We did not estimate the rest-frame continuum at 1500 Å from the spectra because of the lack of good S/N in the continuum in grating spectra. To obtain reliable and homogeneous estimates, we used the available photometry for all sources.

We corrected the obtained UV luminosity densities for dust reddening following the same procedure as for the emission line fluxes as described in Sect. 3.2. We lastly converted
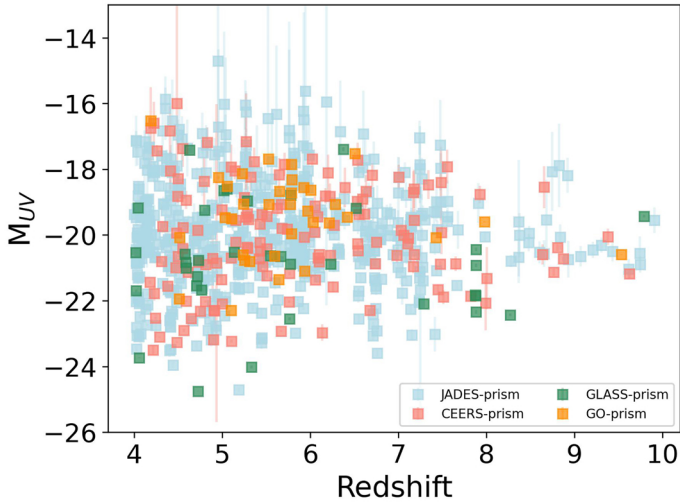
Fig. 3. Distribution of M_{UV} as a function of redshift for the galaxies in the different surveys considered in our sample.

the dust-corrected UV luminosity densities to UV absolute magnitudes, which are analyzed in the following sections. In Fig. 3, we show the distribution of M_{UV} versus redshift. Our sample covers a wide range of M_{UV} (~ 8 mag) with a mean value of $M_{UV} = -20.00$ ($\sigma = 1.61$). In Appendix C we show the distribution of the measured Hα and Hβ emission line flux as a function of both redshift and M_{UV}. We note that our complete sample includes galaxies with $z \lesssim 7$ and $M_{UV} \lesssim -18$, which is the parameter space where our results are more robust.

3.5. Constraints on ξ_{ion}

We estimated the ionizing photon production efficiency in a standard way, considering the model where ξ_{ion} is given by

$$\xi_{ion} = \frac{N(H^0)}{L_{UV}}, \qquad (2)$$

where $N(H^0)$ is the ionizing photon rate in s^{-1} and L_{UV} is the UV luminosity density at 1500 Å. In order to estimate the ionizing photon rate, we use the dust-corrected Hα luminosity when available as:

$$L(H\alpha)[\mathrm{erg\,s^{-1}}] = 1.36 \times 10^{-12} N(H^0)[s^{-1}], \qquad (3)$$

which was derived from Leitherer & Heckman (1995) assuming no ionizing photons escape from the galaxy ($f_{esc} = 0$) and case B recombination. For this conversion factor, it is assumed a Salpeter (1955) initial mass function (IMF) and a gas temperature of 10 000 K for the nebular emission in the evolutionary synthesis models. Alternatively, we use the dust-corrected Hβ luminosity as

$$L(H\beta)[\mathrm{erg\,s^{-1}}] = 4.87 \times 10^{-13} N(H^0)[s^{-1}]. \qquad (4)$$

For galaxies with Hα and Hβ available, we checked that the values are in very good agreement (see Fig. B.1). We assume $f_{esc} = 0$, meaning that all LyC photons are reprocessed into the Balmer lines. The derived ξ_{ion} value can be considered as a lower limit since higher f_{esc} will lead to a higher ξ_{ion}. If Hα or Hβ are detected with S/N < 3, we put an upper 3σ limit in the ξ_{ion} value for that galaxy. We considered an upper limit only if σ is lower than the detection limits of the surveys to avoid overestimating the upper limits. We also considered upper limits on Hα or upper

limits on Hβ only when a limit on Hα is not possible to estimate. We obtained a mean value of $\log(\xi_{ion}\,[\mathrm{Hz\,erg^{-1}}]) = 25.22$ ($\sigma = 0.42$ dex) for the galaxies in the entire sample.

4. Results

4.1. Evolution of ξ_{ion} with redshift

In Fig. 4 we show the evolution of ξ_{ion} with redshift. The magenta squares are the median values in equally distributed redshift bins. For the median values, we considered the upper limits on ξ_{ion} as half their values following the methodology in Calabrò et al. (2024b). In data science, imputation of upper limits with half the detection limit is a common approach, and simulation studies have found that this is a better choice compared to assuming the detection limit itself or a zero value, as it introduces the least bias into the estimates (Beal 2001). The error bars are the observed 1σ scatter within a given redshift bin. We note a shallow trend where the ξ_{ion} increases with redshift from $4 \leq z \leq 10$. Based on the median values, ξ_{ion} increases from $\log(\xi_{ion}\,[\mathrm{Hz\,erg^{-1}}]) = 25.09$ at $z \sim 4.18$ to $\log(\xi_{ion}\,[\mathrm{Hz\,erg^{-1}}]) = 25.28$ at $z \sim 7.14$. The best linear fit of the median values considering the full sample leads to the relation $\log(\xi_{ion}\,[\mathrm{Hz\,erg^{-1}}]) = (0.06 \pm 0.012) \times z + (24.82 \pm 0.07)$. For galaxies at $z \gtrsim 7.14$, the median value of ξ_{ion} is greater than the canonical value with a median value of $\log(\xi_{ion}\,[\mathrm{Hz\,erg^{-1}}]) = 25.28$.

Interestingly, our bins at $z \sim 4$–5 are consistent within 1σ with the values found in Castellano et al. (2023), with the VANDELS galaxies at $2 \leq z \leq 5$ using SED fitting to determine the ξ_{ion} values. They found no significant evolution of ξ_{ion} with redshift, but combining the two results, they suggest an increase in ξ_{ion} from $z \sim 2$ up to $z \sim 10$. This trend also agrees with the relation found in Matthee et al. (2017) based on Hα emitters at $z \sim 2$, which seems to be valid up to $z \sim 12$, according to data from the literature, which are included in Fig. 4. We also compare our results with the recent work from Pahl et al. (2025) with a sample of CEERS and JADES galaxies from $1.06 < z < 6.71$. We find that our results agree with the increase in ξ_{ion} with redshift, but our median values are slightly lower than their observed trend, although consistent within the observed scatter.

We also find that the median values are below the usually assumed canonical value of ξ_{ion}, for the bins at $z < 7$ and then become higher than this value at higher redshift. Given the large scatter, there are individual galaxies in each bin whose ξ_{ion} values are above the canonical values. We do not find a significant difference in the observed trend if we include only galaxies in the complete sample. We still observe the increase in ξ_{ion} with redshift up to $z \sim 6.92$. We remark that the complete subsample extends up to $z \sim 7.5$, which is the z completeness of our study. As we show in Appendix C, the completeness in M_{UV} is up to magnitude ~ -18, which is similar to the completeness of other spectroscopic samples (e.g., Dottorini et al. 2025).

4.2. Relation between ξ_{ion} and M_{UV}

In Fig. 5 we show the relation between ξ_{ion} and M_{UV}. We find an increase in ξ_{ion} with UV magnitude, which is also observed in individual galaxies. This is consistent with other works at $5 \leq z \leq 7$, including galaxies in the emission-line galaxies and intergalactic gas in the EoR (EIGER; Kashino et al. 2023) survey, CEERS, JADES (Mascia et al. 2025), and also with works using photometry to estimate the ξ_{ion} values at comparable redshifts (e.g., Simmonds et al. 2024) where we find a consistent slope. Our best fit of the median values is $\log(\xi_{ion}\,[\mathrm{Hz\,erg^{-1}}]) = (0.15 \pm$
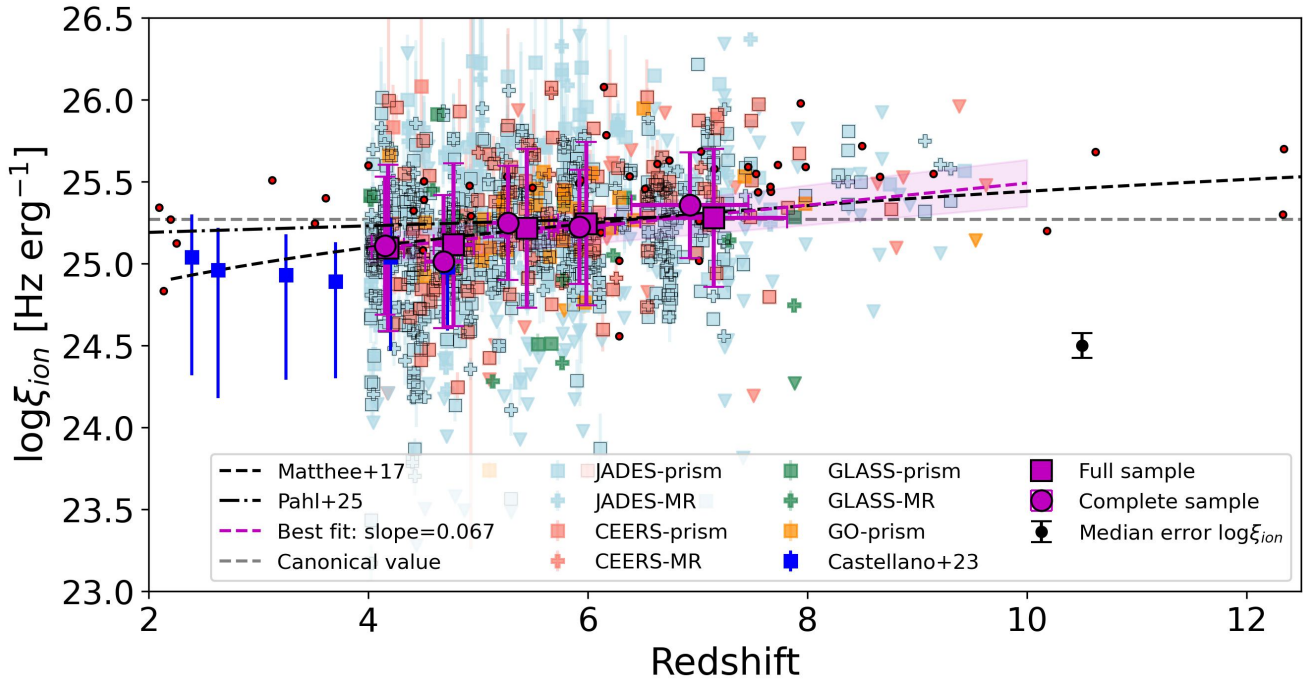
Fig. 4. Redshift evolution of $\xi_{\rm ion}$ for the entire sample. The individual galaxies are in red, light-blue, green, and orange symbols, depending on the parent survey. The symbols with black edges are galaxies in the complete sample. The plus symbols are galaxies based on the grating (MR) configuration, while the square symbols are galaxies observed with the prism configuration. The triangle symbols are upper limits. The magenta symbols are the median values of $\xi_{\rm ion}$ in equally populated bins of redshift. The magenta squares are the median values considering the full sample, while the magenta circles are the median values considering only the complete sample. The blue symbols are average values from Castellano et al. (2023). The red circles are individual galaxies or stacks from literature (Stark et al. 2015; Nakajima et al. 2016; Mármol-Queraltó et al. 2016; Bouwens et al. 2016; Matthee et al. 2017; Stark et al. 2017; Shivaei et al. 2018; Harikane et al. 2018; Vanzella et al. 2018; Faisst et al. 2019; Lam et al. 2019; De Barros et al. 2019; Emami et al. 2020; Nanayakkara et al. 2020; Castellano et al. 2022; Marques-Chaves et al. 2022; Stefanon et al. 2022; Prieto-Lyon et al. 2023; Bunker et al. 2023; Rinaldi et al. 2024; Roberts-Borsani et al. 2024; Mascia et al. 2024a; Saxena et al. 2024; Lin et al. 2024; Álvarez-Márquez et al. 2024; Hsiao et al. 2024; Calabrò et al. 2024a; Vanzella et al. 2024; Zavala et al. 2025). The dashed magenta line is the best fit of the median values of the full sample. The dashed line is the relation from Matthee et al. (2017), and the dotted-dashed line is the relation from Pahl et al. (2025). The canonical value of $\log \xi_{\rm ion}[{\rm Hz\,erg^{-1}}] \approx 25.27$, often assumed in reionization models, is highlighted in a horizontal dashed gray line for reference. The black symbol represents the median error of 0.07 dex in $\log \xi_{\rm ion}$.

$0.008) \times M_{\rm UV} + (28.17 \pm 0.17)$. According to this trend, fainter galaxies tend to show higher $\xi_{\rm ion}$ values compared to brighter galaxies. In particular, galaxies in the fainter bins (median value $\gtrsim -19.36\,{\rm mag}$) show $> \log(\xi_{\rm ion}\ [{\rm Hz\,erg^{-1}}]) = 25.28$ higher than the canonical values. This trend is in the opposite direction compared with recent results from Pahl et al. (2025) and Begley et al. (2025), where they found that fainter galaxies are not the most efficient in producing ionizing photons but the brighter galaxies are. We also note that our relation perfectly agrees with that found in Simmonds et al. (2024) at $z \sim 5$–6. If we consider only the galaxies in the complete sample, we find that the increasing trend is also found. Comparing with the literature, we find that our relation is in agreement with the $\xi_{\rm ion}$ value found recently in a faint source in Vanzella et al. (2024) with $M_{\rm UV} \sim -12$, which suggests faint sources are indeed efficient producers of ionizing photons.

In Fig. 6 we explore if the relation of $\xi_{\rm ion}$ with $M_{\rm UV}$ depends on the redshift. To this aim, we split the sample into three bins of redshifts: $z = 4$–5 (278 galaxies), $z = 5$–7 (366 galaxies), and $z = 7$–10 (117 galaxies). We find that for a given $M_{\rm UV}$, the galaxies with higher redshifts show higher $\xi_{\rm ion}$ values, which is in agreement with the redshift evolution found in Sect. 4.1. The slopes of the relations do not vary sensibly at different redshifts (slopes between 0.15 and 0.21). In

Table 1 we present the parameters of the best linear fits depending on the median redshift. We compare our results with the relations found in recent semi-analytic models with cold gas fractions and star-formation efficiencies obtained from hydrodynamical simulations (Mauerhofer et al. 2025). In particular, we compare our results with the models including an evolving IMF (eIMF) depending on redshift and metallicity, which becomes increasingly top-heavy with redshift or decreasing metallicity. Our results are consistent within 1σ with the increase in $\xi_{\rm ion}$ with the increase in $M_{\rm UV}$ found in the models at redshifts $z \sim 5$–7 (Fig. 14 in Mauerhofer et al. 2025). At $z \sim 9$ the same models suggest a flattening of the relation at $\sim\log(\xi_{\rm ion}\ [{\rm Hz\,erg^{-1}}]) = 25.5$, which is consistent within 1σ with the values we obtained but not with the increasing trend we found in the bin with higher redshifts (median $z = 7.45$). The lower number of galaxies in this bin and the wider redshift range could explain the differences with the models. In any case, our results are consistent with the models with a top-heavy IMF.

4.3. Total ionizing emissivity

We use the relations reported in Table 1 to estimate the total ionizing emissivity $\dot{n}_{\rm ion}$ at the median redshifts in each bin. To do this calculation, we considered the UV luminosity
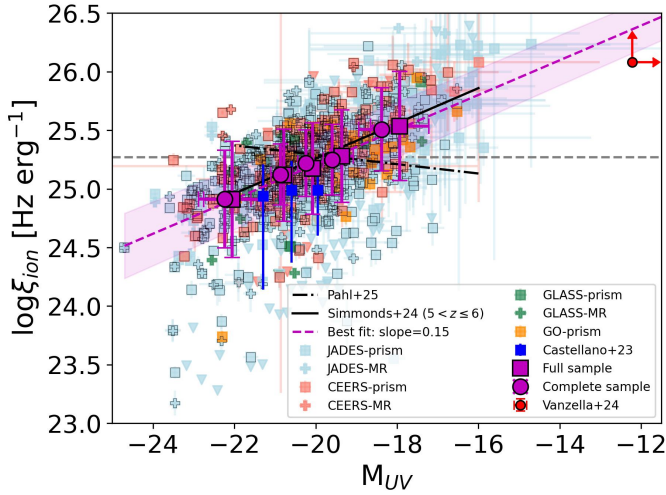
Fig. 5. Relation between ξ_{ion} and M_{UV}. The symbols are the same as in Fig. 4. The dotted-dashed line indicates the relation found in Pahl et al. (2025) for galaxies at $1.06 < z < 6.71$. The solid black line indicates the relation found in Simmonds et al. (2024). The red circle indicates the faint source from Vanzella et al. (2024).

Fig. 6. Relation of ξ_{ion} with M_{UV} in bins of redshift. The red, dark red, and yellow symbols are the median values in the redshift bins. The dashed lines represent models with an eIMF at different redshifts from Mauerhofer et al. (2025). The dashed gray line indicates the canonical value for reference.

Table 1. Parameters of the best fits of the relation between ξ_{ion} and M_{UV} at different redshift, with $\log\xi_{ion} = a \times M_{UV} + b$

Median z	a	b
4.42	0.15 ± 0.02	28.15 ± 0.48
5.79	0.16 ± 0.01	28.49 ± 0.22
7.45	0.21 ± 0.02	29.76 ± 0.36

functions of Bouwens et al. (2021) and a median $f_{esc} = 0.13$ as recently inferred using indirect observational estimates at $z \sim 5-9$ (Mascia et al. 2023, 2024a). This value does not depend substantially on M_{UV}, at least in the magnitude range that can be currently explored. We also considered a maximum value of $\log(\xi_{ion} \, [\mathrm{Hz \, erg^{-1}}]) = 26$, which is in agreement with models of young metal-poor stellar populations (Raiter et al. 2010; Maseda et al. 2020) and simulations of PopIII populations (Lecroq et al. 2025). We integrated the luminosity function from $M_{UV} = -23$ to different faint limits and present the result in Fig. 7 with limits $M_{UV} = -13$ (plotted in red), $M_{UV} = -15$ (in black), and $M_{UV} = -18$ (in green). We performed 1000 Monte Carlo simulations assuming a normal distribution of the parameters of the UV luminosity functions and the best fits in Table 1, keeping the escape fraction constant. The plotted values are the corresponding median values, and the error bars are the 16th and 84th percentiles resulting from the simulations.

We match observational constraints obtained by observing the Lyα forest from Becker & Bolton (2013). Our results are also consistent with IGM evolution models (Madau et al. 1999) and do not support recent claims for a budget-crisis and a too early end of reionization (e.g., Muñoz et al. 2024). We also find that the contribution of faint UV galaxies ($-15 \leq M_{UV} \leq -13$) to the total ionizing emissivity becomes more important at higher redshift, increasing from $\sim 30\%$ at $z \sim 4.4$ to $\sim 47\%$ at $z \sim 7.4$ (Mascia et al. 2024a). On the other hand, the contribution of bright UV galaxies becomes less important at higher redshift, decreasing from $\sim 26\%$ at $z \sim 4.4$ to $\sim 9\%$ at $z \sim 7.4$. These results indicate that faint galaxies are the dominant sources of ionizing photons during the EoR.
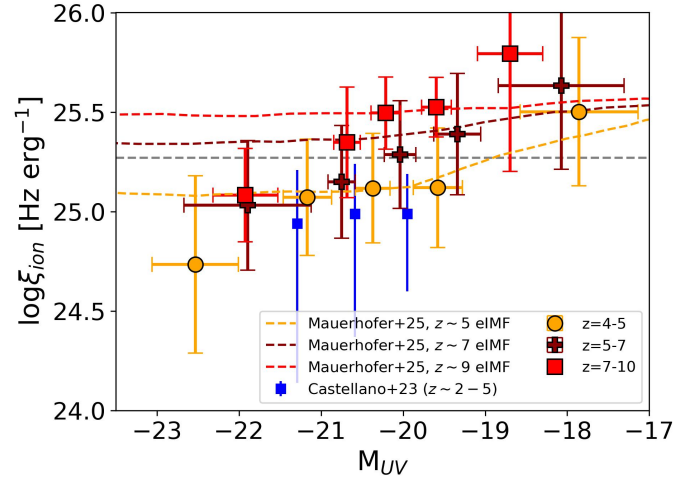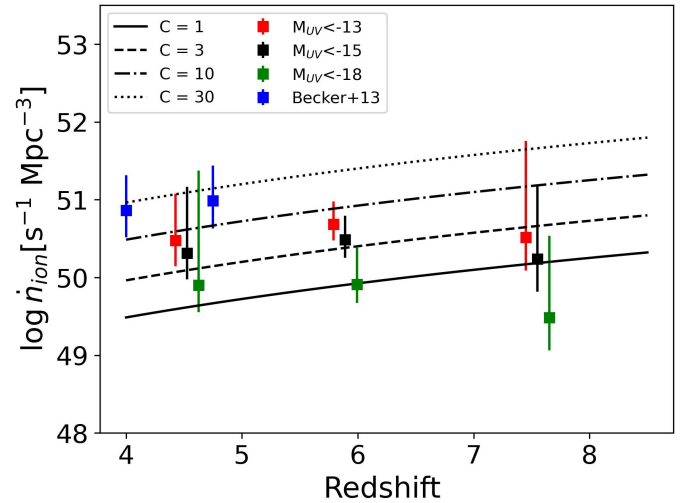

Fig. 7. Evolution of the total ionizing emissivity. The red, black, and green squares are our estimations after integrating from $M_{UV} = -23$ to $M_{UV} = -13$, $M_{UV} = -15$, and $M_{UV} = -18$, respectively. The black and green squares are shifted by 0.1 and 0.2 in redshift, respectively, for better visualization. The different lines represent IGM evolution models from Madau et al. (1999) for different ionized hydrogen clumping factors C. The blue squares are observational constraints obtained by observing the Lyα forest from Becker & Bolton (2013).

4.4. Dependence of ξ_{ion} on the physical properties

In this section we present our results on the relation between ξ_{ion} and the physical properties obtained based on SED fitting. On the top panel in Fig. 8 we show the relation between ξ_{ion} and the stellar mass. Based on the median values in stellar mass bins, we find a clear decrease in ξ_{ion} with stellar mass. The best fit shown in Fig. 8 considers the median values. The best fit of the relation that we found is $\log(\xi_{ion} \, [\mathrm{Hz \, erg^{-1}}]) = (-0.35 \pm 0.01) \times \log(M_\star/M_\odot) + (28.12 \pm 0.11)$. This trend is in agreement with the one observed in VANDELS galaxies at lower redshifts (Castellano et al. 2023). We note a small offset, with the VANDELS sources showing slightly higher ξ_{ion} values for a given
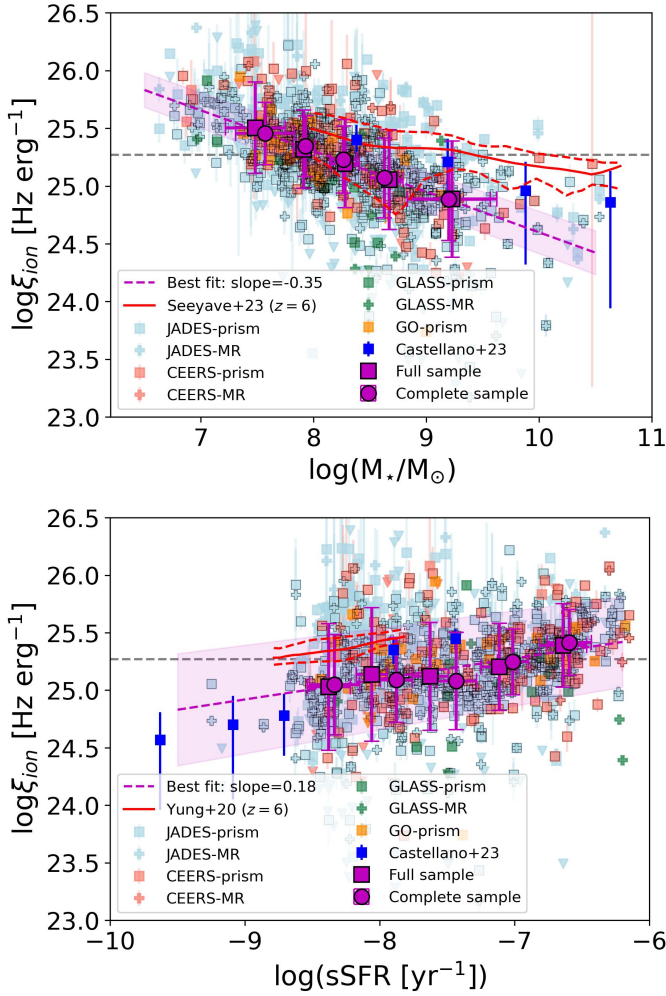
Fig. 8. Relation of ξ_{ion} with physical properties of the galaxies. The top panel indicates the relation between ξ_{ion} and stellar mass, while the bottom panel indicates the relation between ξ_{ion} and the specific star-formation rate. The symbols are the same as in Fig. 4. In the top panel, the solid red line indicates the trend from the FLARES simulation at $z = 6$ (Seeyave et al. 2023), and the dashed red lines indicate their 3σ scatter. In the bottom panel, the solid red line represents the trend from the simulations in Yung et al. (2020b) at $z = 6$. The dashed red lines are the 16th and 84th percentiles.
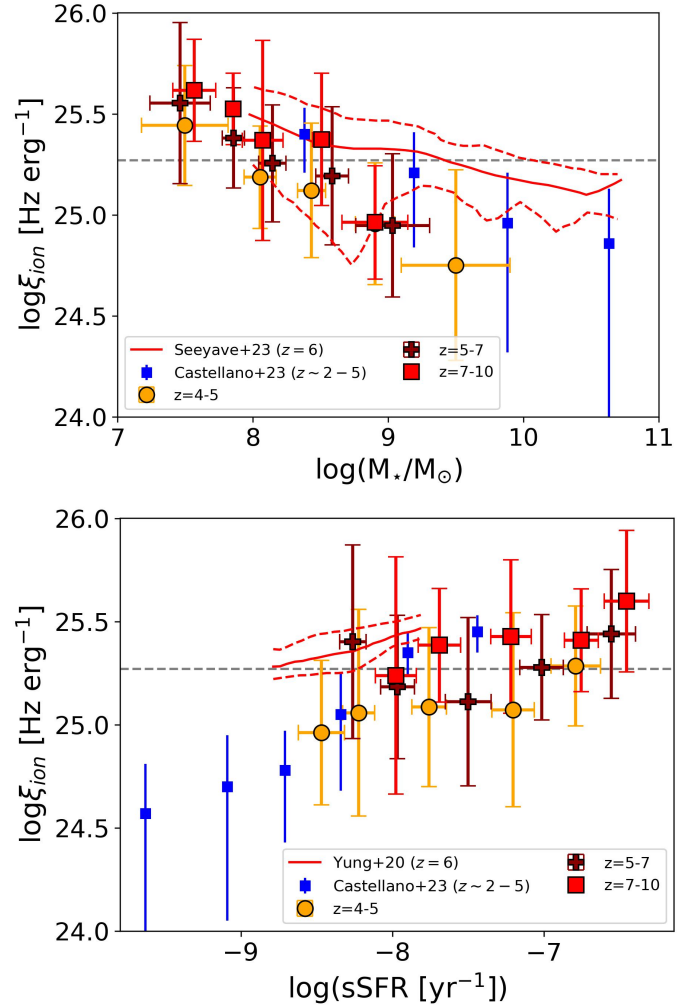
Fig. 9. Relation of ξ_{ion} with physical properties of the galaxies in bins of redshift. The red, dark red, and yellow symbols are the median values in redshift bins. The dashed gray line is the canonical value for reference.

stellar mass; however, this could be an effect of the method used to estimate ξ_{ion}, since we are using Balmer lines. We note that in Castellano et al. (2023) SED modeling with BPASS was used (for more details, see in Sect. 4.5), and that their sample is complete for galaxies with stellar masses $>10^{9.5} M_\odot$ which could lead to the offsets observed in the lower mass bins.

This decreasing trend is also observed in Simmonds et al. (2024) using NIRCam photometry for a sample of $\sim$670 galaxies at $z \sim 3.9$–8.9. Interestingly, the two bins with lower stellar mass (median value $\lesssim 10^{7.91} M_\odot$) show a median $>\log(\xi_{ion} [\mathrm{Hz\,erg}^{-1}]) = 25.31$ above the canonical value, which indicates that galaxies with lower stellar masses than this value tend to be efficient in producing ionizing photons. We also compare the trend we find with the results from simulations. In particular, we compare with the results from Seeyave et al. (2023) based on the FLARES simulation. They find a shallower decrease in ξ_{ion} with redshift, with higher values of ξ_{ion} for a given stellar mass. Our values are consistent with the 3σ scatter of their rela-

tion, in particular for low stellar masses. The differences could be attributed to using BPASS models in the simulations. According to Seeyave et al. (2023), the decreasing trend of ξ_{ion} with stellar mass is due to the combined effects of increasing age and metallicity with increasing stellar mass, with metallicity likely playing a bigger role (compared to age) due to the weaker evolution of age with stellar mass.

On the bottom panel in Fig. 8 we show the relation between ξ_{ion} and the sSFR. Based on the median values in sSFR bins, we find a clear increase in ξ_{ion} with sSFR. The best fit of the relation that we found is $\log(\xi_{ion} [\mathrm{Hz\,erg}^{-1}]) = (0.18 \pm 0.04) \times \log(\mathrm{sSFR[yr^{-1}]}) + (26.53 \pm 0.30)$. This trend is also clear in individual galaxies. This trend is also in agreement with the one observed in VANDELS galaxies at lower redshifts (Castellano et al. 2023) in the common sSFR range covered by the two studies. Similar to the relation between ξ_{ion} and stellar mass, we note that the bin with higher sSFR (median value $\sim 10^{-6.64} \mathrm{yr}^{-1}$) shows a median $\log(\xi_{ion} [\mathrm{Hz\,erg}^{-1}]) = 25.38$, which is above the canonical value. This indicates that galaxies with sSFR higher than this value tend to be efficient producers of ionizing photons. Considering the complete sample, we note that galaxies with $\sim 10^{-6.59} \mathrm{yr}^{-1}$) tend to show ξ_{ion} above the canonical values as well, with a median value of $\log(\xi_{ion}$

[Hz erg^{-1}]) = 25.39. Comparing our results with the simulations from Yung et al. (2020b), we find a similar trend of increasing ξ_{ion} with increasing sSFR, but with an offset. Despite this offset, the slope we find is similar to the one in the simulations.

In Fig. 9, we explore if the relations of ξ_{ion} with stellar mass and sSFR depend on redshift. To this aim, we split the sample into the same three bins of redshifts as in Sect. 4.2. In Fig. 9, we show the median values of each bin. We find that for a given stellar mass, the galaxies with higher redshifts show higher ξ_{ion} values, which is in agreement with the redshift evolution found in Sect. 4.1. Similar results are found with sSFR, with the galaxies in the bin $z = 7-10$ showing the highest ξ_{ion} values. The slopes of the relations do not vary significantly at different redshifts (slopes between -0.33 and -0.44 for the relation between ξ_{ion} and stellar mass, and slopes between 0.05 and 0.18 for the relation between ξ_{ion} and sSFR), implying that the physical conditions leading to photon production in galaxies remain essentially the same across cosmic epochs i.e., for the same metallicity and ages, the efficiency is the same.

4.5. Relation between ξ_{ion} and EW([OIII])

The EW([OIII]) has been often used as a proxy for ξ_{ion}. For example, Chevallard et al. (2018) found the relation marked with the solid line in Fig. 10 using a sample of 10 nearby analogs of primeval galaxies, which was then used in several works (Castellano et al. 2023). In Fig. 10, we show the relation between ξ_{ion} and the EW([OIII]) for our sample. For the estimation of the EWs, we considered the continuum measured directly from the spectra based on Gaussian fitting. We find an increase in ξ_{ion} with the EW([OIII]), where the more efficient ionizing photon producers are the galaxies that show the higher EW([OIII]). In particular, we show that the galaxies in the bins with higher EWs (median value $\gtrsim 1800$ Å) show values of $> \log(\xi_{ion}$ [Hz erg^{-1}]) = 25.40 above the canonical values. The best fit of the median values results in the relation $\log(\xi_{ion}$ [Hz erg^{-1}]) = $(0.43 \pm 0.02) \times \log($EW([OIII])[Å]$) + (23.99 \pm 0.05)$. Compared to our trend, the Chevallard et al. (2018) relation is much steeper and tends to overpredict ξ_{ion} values for the most extreme cases of EW([OIII]) and at the same time underpredict the ξ_{ion} values in the cases with moderate EWs. A somewhat better agreement is found with the relation derived by Tang et al. (2019) for a sample of ~200 intense [OIII] emitters at $1.3 < z < 2.4$. We find good agreement in the bins with lower EWs, while in the more intense cases, our values tend to be lower than those predicted by these authors. Compared to the recent work by Pahl et al. (2025), we find slightly higher average values of ξ_{ion} for a given EW. Nevertheless, the slope of the relation is consistent.

We note that these offsets in the relations could also be the origin for the discrepancies observed in Fig. 8 when comparing our work to Castellano et al. (2023). Their ξ_{ion} values are estimated using BEAGLE (Chevallard & Charlot 2016) and are consistent with the Chevallard et al. (2018) relation, which we found tends to overpredict the ξ_{ion} for a given EW, in particular in galaxies with high EWs.

Recently, Laseter et al. (2024) found that modest [OIII] emitters (EW~300–600 Å) may also show high values of ξ_{ion} as we also show in individual galaxies in Fig. 10. One of the drivers of this effect could be the low metallicity in the systems where the EW([OIII]) is suppressed, but the fluxes of Balmer lines remain elevated. We analyze the relation of ξ_{ion} with gas-phase metallicity in Sect. 4.6. This dependency on gas-phase metallicity would
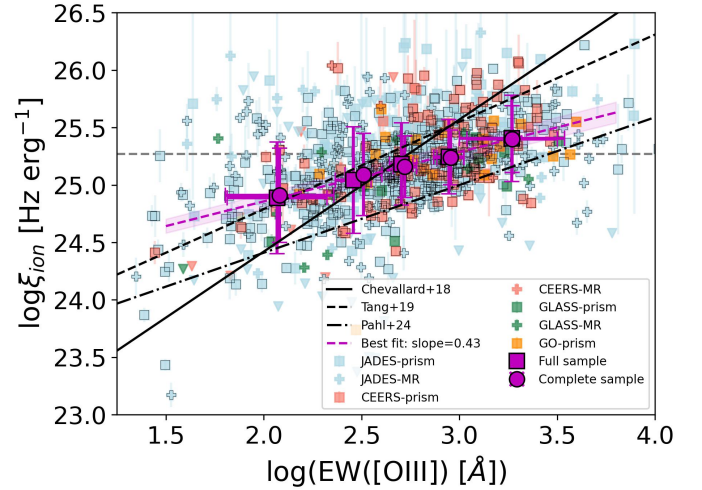

Fig. 10. Relation between ξ_{ion} and EW([OIII]). The symbols are the same as in Fig. 4. The solid black line indicates the local relation from Chevallard et al. (2018). The dashed line indicates the relation from Tang et al. (2019) at $1.3 < z < 2.4$. The dotted-dashed line indicates the relation found in Pahl et al. (2025) for galaxies at $1.06 < z < 6.71$.

limit the use of [OIII] as a sole tracer of high z efficient ionizing systems.

4.6. Relation of ξ_{ion} with O32 and gas-phase metallicity

In Fig. 11, we show the relation between ξ_{ion} and O32=log([OIII]/[OII]). We also include the limit O32 > 0.69 from Flury et al. (2022) to separate strong LyC leakers found in the low redshift LyC survey galaxies. We find an increasing trend where the galaxies with higher O32 values show the highest ξ_{ion} values. The best fit of the median values results in the relation $\log(\xi_{ion}$ [Hz erg^{-1}]) = $(0.55 \pm 0.07) \times \log($[OIII]/[OII]$) + (24.77 \pm 0.04)$. The bin with the higher O32 values (~0.92) is above the threshold for strong LyC leakers, and it shows a median value $\log(\xi_{ion}$ [Hz erg^{-1}]) = 25.27, slightly above the canonical value. A similar trend was found in Shen et al. (2025) for galaxies at $z \sim 2-3$. We find a similar slope of the relation compared to their median values, but our ξ_{ion} values are slightly lower for a given O32 value. Since a high O32 ratio is one of the proposed proxies for a high escape of LyC radiation (Flury et al. 2022; Mascia et al. 2024a), our findings could imply that galaxies with high ionizing photon production efficiency are also those where the LyC escape is high. This has important implications for determining which sources contributed most to reionization. However, a high O32 is actually a necessary but not sufficient condition for a high escape fraction, and some authors actually find that at least for some classes of galaxies (e.g., Lyα emitters), production and escape of ionizing photons are anticorrelated (Saxena et al. 2024). We plan to investigate these links further in future works.

In Fig. 12, we show the relation between ξ_{ion} and gas-phase metallicity. We estimate the metallicity from the R23 = ([OIII]$\lambda\lambda$4959,5007+[OII]$\lambda\lambda$3727,3729)/Hβ calibration presented in Sanders et al. (2024) for galaxies at $z = 2.1-8.7$. Given that this relation is bivaluated, we also used the O32 calibration in Sanders et al. (2024). We consider as metallicity estimation the metallicity from the R23 calibration that is closer to the value from the O32 calibration. We find a shal-
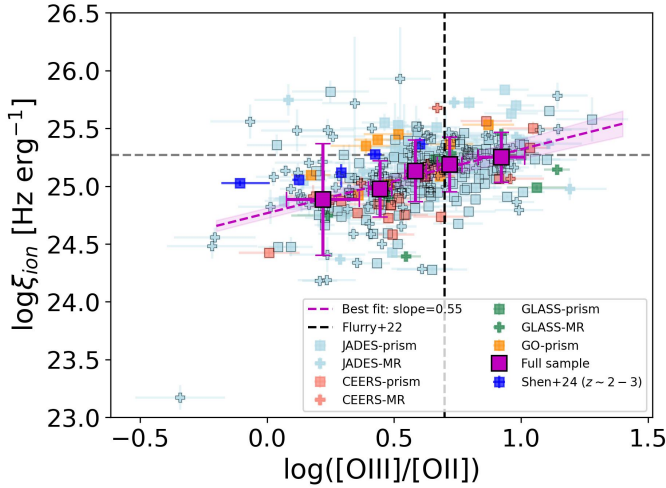
Fig. 11. Relation between ξ_{ion} and O32. The symbols are the same as in Fig. 4. The blue squares indicate the median values from Shen et al. (2025) for galaxies at $z \sim 2-3$. The vertical line indicates the demarcation line between strong and weak leakers from Flury et al. (2022).
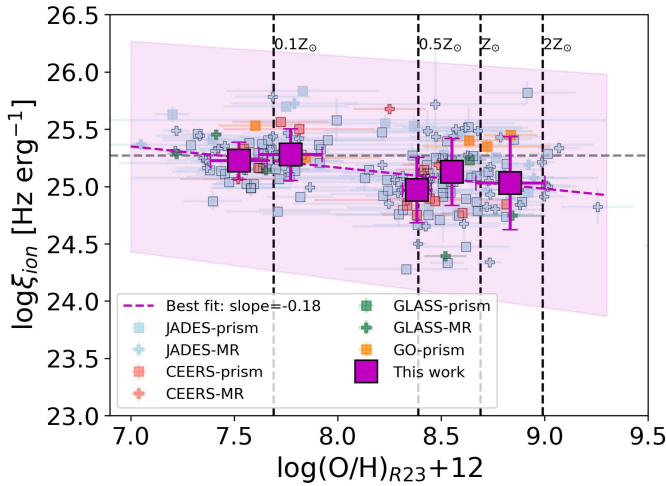

Fig. 12. Relation between ξ_{ion} and gas-phase metallicity. The symbols are the same as in Fig. 4.

low decreasing trend with metallicity, with the metal-poor galaxies showing the higher ξ_{ion} values. The best fit of the median values results in the relation $\log(\xi_{ion}~[\mathrm{Hz\,erg^{-1}}]) = (-0.18 \pm 0.08) \times (\log(\mathrm{O/H})+12)+(26.64 \pm 0.69)$. According to the best fit of the median values, galaxies with metallicities $\lesssim 10\%$ solar tend to show ξ_{ion} values above the canonical value and are efficient in producing LyC photons. We note that this relation is consistent with a flat slope at 3σ, and a larger sample would be needed to better constrain the dependency of ξ_{ion} on metallicity.

5. Summary and conclusions

We selected a sample of 761 galaxies at $z = 4-10$ with NIRSpec spectra in four JWST surveys (CEERS, JADES, GLASS, and GO-3073) in this large study of ξ_{ion} conducted via spectroscopy. We estimated their physical properties using available JWST and HST photometry for performing SED fitting using BAGPIPES (Carnall et al. 2018), assuming a delayed exponential model for the SFH. We constrained the ξ_{ion} values based on Balmer lines

(Hα or Hβ) and estimated the gas-phase metallicity using R23 and O32 calibrations for high z sources. We investigated the evolution of ξ_{ion} with redshift and its relation to the physical properties of the galaxies. Our main results are the following:

- We find an evolution of the ionizing photon production efficiency of star-forming galaxies with higher values of ξ_{ion} at higher redshifts. The evolution is mild, with the best linear relation given by $\log(\xi_{ion}~[\mathrm{Hz\,erg^{-1}}]) = (0.06 \pm 0.012) \times z+(24.82 \pm 0.07)$. This trend is consistent with other results at lower redshifts. According to this relation, a median value of $\log(\xi_{ion}~[\mathrm{Hz\,erg^{-1}}]) = 25.12$ is inferred at $z = 4.5$, while a median value of $\log(\xi_{ion}~[\mathrm{Hz\,erg^{-1}}]) = 25.32$ is inferred at $z = 7.5$.
- We find an increase in ξ_{ion} with increasing M_{UV}. The best fit results in the relation $\log(\xi_{ion}~[\mathrm{Hz\,erg^{-1}}]) = (0.15 \pm 0.008) \times M_{UV}+(28.17 \pm 0.17)$. We also evaluated the ξ_{ion} versus M_{UV} relation in separate redshift bins and found that the slopes of the different relations stay constant, although with increasing offset. The relations are consistent with the predictions of recent models, with the eIMF becoming top-heavy at higher redshifts and lower metallicity.
- Assuming our values of ξ_{ion} as a function of M_{UV} and redshift, and a mean escape fraction of 0.13 as recently derived by Mascia et al. (2025), we calculated the evolution of the total ionizing emissivity. Our results show that galaxies can sustain reionization, provided that the clumpiness factor does not exceed 10 and is consistent with low redshift constraints by the Lyα forest. We also find that faint UV galaxies ($-15 \leq M_{UV} \leq -13$) are the main contributors of ionizing photons in the early stages of reionization.
- We find a decrease in ξ_{ion} values with increasing $M_\star$ with the best fit resulting in the relation $\log(\xi_{ion}~[\mathrm{Hz\,erg^{-1}}]) = (-0.35 \pm 0.01) \times \log(M_\star/M_\odot)+(28.12 \pm 0.11)$. We find an increase in ξ_{ion} with increasing sSFR, similar to other studies at lower redshifts. The best fit results in the relation $\log(\xi_{ion}~[\mathrm{Hz\,erg^{-1}}]) = (0.18 \pm 0.04) \times \log(\mathrm{sSFR}[\mathrm{yr^{-1}}])+(26.53 \pm 0.30)$. This indicates that low-mass, faint in the UV, and with high levels of sSFRs galaxies tend to be efficient in producing ionizing photons. The slopes of the above relations do not significantly change with redshift, implying that the conditions for photon production do not change and that the redshift evolution is only due to the different statistical properties of populations at each redshift.
- We find an increase in ξ_{ion} with EW(O[III]). The best fit results in the relation $\log(\xi_{ion}~[\mathrm{Hz\,erg^{-1}}]) = (0.43 \pm 0.02) \times \log(\mathrm{EW([OIII])[\AA]})+(23.99 \pm 0.05)$. Compared to our trend, the widely used relation found by Chevallard et al. (2018) is much steeper and tends to overpredict the ξ_{ion} values in the most extreme cases of EW([OIII]) and, to the contrary, underpredict the ξ_{ion} values in the cases with moderate EWs. We instead find better agreement with the relation proposed by Tang et al. (2019), at least in the bins with lower EWs, while in the bins with higher EWs, our ξ_{ion} values are lower.
- We find an increase in ξ_{ion} with O32 ratio. The best fit results in the relation $\log(\xi_{ion}~[\mathrm{Hz\,erg^{-1}}]) = (0.55 \pm 0.07) \times \log([\mathrm{OIII}]/[\mathrm{OII}])+(24.77 \pm 0.04)$. Since O32 is one of the most used proxies for a high escape fraction of LyC photons, this could imply that leakers are also efficient in producing ionizing photons, in contrast to some previous findings.
- Finally, we find a decrease in ξ_{ion} with gas-phase metallicity. The best fit results in the relation $\log(\xi_{ion}~[\mathrm{Hz\,erg^{-1}}]) = (-0.18 \pm 0.08) \times (\log(\mathrm{O/H})+12)+(26.64 \pm 0.69)$. The rather shallow relation indicates that metallicity does not

play such a key role in determining the photon production efficiency.

Overall, we find that faint low-mass galaxies with high levels of sSFRs present the best conditions for an efficient production of ionizing photons, while low metallicity seems to play a more marginal role in setting such conditions, given the shallow trend observed. We also find indications that galaxies with high photon production efficiency may also be those in which the conditions for high leakage of such photons are present, since they share properties similar to low redshift LyC leakers – namely, high O32, faint UV magnitudes, and low-stellar masses. Such galaxies could therefore be primarily responsible for cosmic reionization: we plan to further investigate the link between ionizing photon production and escape in a follow-up study. In general, although we do find that high redshift galaxies have higher ξ_{ion} compared to the low redshift sources with similar properties, our median values for the galaxy population during the EoR are not as extreme as those found by other authors (e.g., Maseda et al. 2020; Prieto-Lyon et al. 2023; Atek et al. 2024; Saxena et al. 2024). In agreement with other authors (e.g., Simmonds et al. 2024), our results, therefore, do not support recent claims of a budget crisis, i.e. that the total ionizing photons generated by galaxies are much higher than previously thought. Such a scenario, together with significant escape fractions, could provide enough photons to end reionization too early, which would be in contrast to Lyman α forest results (Muñoz et al. 2024).

References

Álvarez-Márquez, J., Colina, L., Crespo Gómez, A., et al. 2024, A&A, 686, A85
Arrabal Haro, P., Dickinson, M., Finkelstein, S. L., et al. 2023, ApJ, 951, L22
Asplund, M., Grevesse, N., Sauval, A. J., & Scott, P. 2009, ARA&A, 47, 481
Atek, H., Labbé, I., Furtak, L. J., et al. 2024, Nature, 626, 975
Backhaus, B. E., Trump, J. R., Cleri, N. J., et al. 2022, ApJ, 926, 161
Bagley, M. B., Finkelstein, S. L., Koekemoer, A. M., et al. 2023, ApJ, 946, L12
Beal, S. L. 2001, J. Pharmacokinetics Pharmacodynamicsp, 28, 504
Becker, G. D., & Bolton, J. S. 2013, MNRAS, 436, 1023
Begley, R., McLure, R. J., Cullen, F., et al. 2025, MNRAS, 537, 3245
Beichman, C. A., Rieke, M., Eisenstein, D., et al. 2012, in Space Telescopes and Instrumentation 2012: Optical, Infrared, and Millimeter Wave, eds. M. C. Clampin, G. G. Fazio, H. A. MacEwen, & J. M. Oschmann, SPIE Conf. Ser., 8442, 84422N
Bergamini, P., Acebron, A., Grillo, C., et al. 2023, ApJ, 952, 84
Bertin, E., & Arnouts, S. 1996, A&AS, 117, 393
Bosman, S. E. I., Davies, F. B., Becker, G. D., et al. 2022, MNRAS, 514, 55
Bouwens, R. J., Smit, R., Labbé, I., et al. 2016, ApJ, 831, 176
Bouwens, R. J., Oesch, P. A., Stefanon, M., et al. 2021, AJ, 162, 47

Brooks, M., Simons, R. C., Trump, J. R., et al. 2024, arXiv e-prints [arXiv:2410.07340]
Bruzual, G., & Charlot, S. 2003, MNRAS, 344, 1000
Bunker, A. J., Saxena, A., Cameron, A. J., et al. 2023, A&A, 677, A88
Bushouse, H., Eisenhamer, J., Dencheva, N., et al. 2022, https://doi.org/10.5281/zenodo.7041998
Calabrò, A., Castellano, M., Zavala, J. A., et al. 2024a, ApJ, 975, 245
Calabrò, A., Pentericci, L., Santini, P., et al. 2024b, A&A, 690, A290
Calzetti, D., Armus, L., Bohlin, R. C., et al. 2000, ApJ, 533, 682
Carnall, A. C., McLure, R. J., Dunlop, J. S., & Davé, R. 2018, MNRAS, 480, 4379
Castellano, M., Pentericci, L., Cupani, G., et al. 2022, A&A, 662, A115
Castellano, M., Belfiori, D., Pentericci, L., et al. 2023, A&A, 675, A121
Chevallard, J., & Charlot, S. 2016, MNRAS, 462, 1415
Chevallard, J., Charlot, S., Senchyna, P., et al. 2018, MNRAS, 479, 3264
Coil, A. L., Aird, J., Reddy, N., et al. 2015, ApJ, 801, 35
De Barros, S., Oesch, P. A., Labbé, I., et al. 2019, MNRAS, 489, 2355
D'Eugenio, F., Cameron, A. J., Scholtz, J., et al. 2025, ApJS, 277, 4
Dottorini, D., Calabrò, A., Pentericci, L., et al. 2025, A&A, 698, A234
Eisenstein, D. J., Johnson, B. D., Robertson, B., et al. 2023, ApJS, submitted, [arXiv:2310.12340]
Emami, N., Siana, B., Alavi, A., et al. 2020, ApJ, 895, 116
Faisst, A. L., Capak, P. L., Emami, N., Tacchella, S., & Larson, K. L. 2019, ApJ, 884, 133
Fan, X., Strauss, M. A., Becker, R. H., et al. 2006, AJ, 132, 117
Fernández, V., Amorín, R., Firpo, V., & Morisset, C. 2024, A&A, 688, A69
Finkelstein, S. L., D'Aloisio, A., Paardekooper, J.-P., et al. 2019, ApJ, 879, 36
Finkelstein, S. L., Bagley, M. B., Ferguson, H. C., et al. 2023, ApJ, 946, L13
Finkelstein, S. L., Bagley, M. B., Arrabal Haro, P., et al. 2025, ApJ, 983, L4
Flury, S. R., Jaskot, A. E., Ferguson, H. C., et al. 2022, ApJ, 930, 126
Gardner, J. P., Mather, J. C., Clampin, M., et al. 2006, Space Sci. Rev., 123, 485
Gardner, J. P., Mather, J. C., Abbott, R., et al. 2023, PASP, 135, 068001
Grogin, N. A., Kocevski, D. D., Faber, S. M., et al. 2011, ApJS, 197, 35
Harikane, Y., Ouchi, M., Shibuya, T., et al. 2018, ApJ, 859, 84
Harris, C. R., Millman, K. J., van der Walt, S. J., et al. 2020, Nature, 585, 357
Hsiao, T. Y.-Y., Abdurro'uf, Coe, D., et al. 2024, ApJ, 973, 8
Hunter, J. D. 2007, Comput. Sci. Eng., 9, 90
Iyer, K., Gawiser, E., Davé, R., et al. 2018, ApJ, 866, 120
Jakobsen, P., Ferruit, P., Alves de Oliveira, C., et al. 2022, A&A, 661, A80
Juneau, S., Bournaud, F., Charlot, S., et al. 2014, ApJ, 788, 88
Kashino, D., Lilly, S. J., Matthee, J., et al. 2023, ApJ, 950, 66
Koekemoer, A. M., Faber, S. M., Ferguson, H. C., et al. 2011, ApJS, 197, 36
Lam, D., Bouwens, R. J., Labbé, I., et al. 2019, A&A, 627, A164
Laseter, I. H., Maseda, M. V., Simmonds, C., et al. 2024, arXiv e-prints [arXiv:2412.04542]
Lecroq, M., Charlot, S., Bressan, A., et al. 2025, A&A, 695, A17
Leitherer, C., & Heckman, T. M. 1995, ApJS, 96, 9
Lin, Y.-H., Scarlata, C., Williams, H., et al. 2024, MNRAS, 527, 4173
Llerena, M., Amorín, R., Cullen, F., et al. 2022, A&A, 659, A16
Madau, P., Haardt, F., & Rees, M. J. 1999, ApJ, 514, 648
Madau, P., Giallongo, E., Grazian, A., & Haardt, F. 2024, ApJ, 971, 75
Maiolino, R., Scholtz, J., Curtis-Lake, E., et al. 2024, A&A, 691, A145
Mármol-Queraltó, E., McLure, R. J., Cullen, F., et al. 2016, MNRAS, 460, 3587
Marques-Chaves, R., Schaerer, D., Álvarez-Márquez, J., et al. 2022, MNRAS, 517, 2972
Mascia, S., Pentericci, L., Calabrò, A., et al. 2023, A&A, 672, A155
Mascia, S., Pentericci, L., Calabrò, A., et al. 2024a, A&A, 685, A3
Mascia, S., Roberts-Borsani, G., Treu, T., et al. 2024b, A&A, 690, A2
Mascia, S., Pentericci, L., Llerena, M., et al. 2025, A&A, submitted, [arXiv:2501.08268]
Maseda, M. V., Bacon, R., Lam, D., et al. 2020, MNRAS, 493, 5120
Matthee, J., Sobral, D., Best, P., et al. 2017, MNRAS, 465, 3637
Mauerhofer, V., Dayal, P., Haehnelt, M. G., et al. 2025, A&A, 696, A157
Merlin, E., Santini, P., Paris, D., et al. 2024, A&A, 691, A240
Muñoz, J. B., Mirocha, J., Chisholm, J., Furlanetto, S. R., & Mason, C. 2024, MNRAS, 535, L37
Naidu, R. P., Tacchella, S., Mason, C. A., et al. 2020, ApJ, 892, 109
Nakajima, K., Ellis, R. S., Iwata, I., et al. 2016, ApJ, 831, L9
Nanayakkara, T., Brinchmann, J., Glazebrook, K., et al. 2020, ApJ, 889, 180
Napolitano, L., Castellano, M., Pentericci, L., et al. 2025, A&A, 693, A50
Oke, J. B., & Gunn, J. E. 1983, ApJ, 266, 713
Pahl, A., Topping, M. W., Shapley, A., et al. 2025, ApJ, 981, 134
Prieto-Lyon, G., Strait, V., Mason, C. A., et al. 2023, A&A, 672, A186
Raiter, A., Schaerer, D., & Fosbury, R. A. E. 2010, A&A, 523, A64
Reddy, N. A., Topping, M. W., Shapley, A. E., et al. 2022, ApJ, 926, 31
Rinaldi, P., Caputi, K. I., Iani, E., et al. 2024, ApJ, 969, 12
Roberts-Borsani, G., Treu, T., Shapley, A., et al. 2024, ApJ, 976, 193

Robertson, B. E. 2022, ARA&A, 60, 121
Robertson, B. E., Furlanetto, S. R., Schneider, E., et al. 2013, ApJ, 768, 71
Rosdahl, J., Katz, H., Blaizot, J., et al. 2018, MNRAS, 479, 994
Salpeter, E. E. 1955, ApJ, 121, 161
Sanders, R. L., Shapley, A. E., Topping, M. W., Reddy, N. A., & Brammer, G. B. 2024, ApJ, 962, 24
Saxena, A., Bunker, A. J., Jones, G. C., et al. 2024, A&A, 684, A84
Seeyave, L. T. C., Wilkins, S. M., Kuusisto, J. K., et al. 2023, MNRAS, 525, 2422
Shen, L., Papovich, C., Matharu, J., et al. 2025, ApJ, 980, L45
Shivaei, I., Reddy, N. A., Siana, B., et al. 2018, ApJ, 855, 42
Simmonds, C., Tacchella, S., Hainline, K., et al. 2024, MNRAS, 527, 6139
Speagle, J. S., Steinhardt, C. L., Capak, P. L., & Silverman, J. D. 2014, ApJS, 214, 15
Stanton, T. M., Cullen, F., McLure, R. J., et al. 2024, MNRAS, 532, 3102
Stark, D. P., Walth, G., Charlot, S., et al. 2015, MNRAS, 454, 1393
Stark, D. P., Ellis, R. S., Charlot, S., et al. 2017, MNRAS, 464, 469
Stefanon, M., Bouwens, R. J., Illingworth, G. D., et al. 2022, ApJ, 935, 94
Tang, M., Stark, D. P., Chevallard, J., & Charlot, S. 2019, MNRAS, 489, 2572
Tang, M., Stark, D. P., Chen, Z., et al. 2023, MNRAS, 526, 1657
Treu, T., Roberts-Borsani, G., Bradac, M., et al. 2022, ApJ, 935, 110
Vanzella, E., Nonino, M., Cupani, G., et al. 2018, MNRAS, 476, L15
Vanzella, E., Loiacono, F., Messa, M., et al. 2024, A&A, 691, A251
Wright, G. S., Wright, D., Goodson, G. B., et al. 2015, PASP, 127, 595
Yang, J., Wang, F., Fan, X., et al. 2020, ApJ, 904, 26
Yung, L. Y. A., Somerville, R. S., Finkelstein, S. L., et al. 2020a, MNRAS, 496, 4574
Yung, L. Y. A., Somerville, R. S., Popping, G., & Finkelstein, S. L. 2020b, MNRAS, 494, 1002
Zavala, J. A., Castellano, M., Akins, H. B., et al. 2025, Nat. Astron., 9, 155

[1] INAF – Osservatorio Astronomico di Roma, Via di Frascati 33, 00078 Monte Porzio Catone, Italy
[2] Dipartimento di Fisica, Università di Roma Sapienza, Città Universitaria di Roma – Sapienza, Piazzale Aldo Moro, 2, 00185 Roma, Italy
[3] Institute of Science and Technology Austria (ISTA), Am Campus 1, A-3400 Klosterneuburg, Austria
[4] Instituto de Astrofísica de Andalucía (CSIC), Apartado 3004, 18080 Granada, Spain
[5] Department of Astronomy and Astrophysics, The Pennsylvania State University, University Park,, PA 16802, USA
[6] Institute for Computational and Data Sciences, The Pennsylvania State University, University Park,, PA 16802, USA
[7] Institute for Gravitation and the Cosmos, The Pennsylvania State University, University Park,, PA 16802, USA
[8] University of Massachusetts Amherst, 710 North Pleasant Street, Amherst, MA 01003-9305, USA
[9] Space Telescope Science Institute, 3700 San Martin Drive, Baltimore, MD 21218, USA
[10] Institute of Physics, Laboratory of Galaxy Evolution, Ecole Polytechnique Fédérale de Lausanne (EPFL), Observatoire de Sauverny, 1290 Versoix, Switzerland
[11] Centre for Astrophysics and Supercomputing, Swinburne University of Technology, PO Box 218, Hawthorn, VIC 3122, Australia
[12] Center for Astrophysics | Harvard & Smithsonian, Cambridge, MA 02138, USA
[13] Black Hole Initiative, Harvard University, Cambridge, MA 02138, USA
[14] Department of Physics and Astronomy, Texas A&M University,, College Station TX 77843-4242, USA
[15] Astronomy Centre, University of Sussex, Falmer, Brighton BN1 9QH, UK
[16] Institute of Space Sciences and Astronomy, University of Malta, Msida, MSD 2080, Malta
[17] National Radio Astronomy Observatory, 520 Edgemont Road, Charlottesville, VA 22903, USA
[18] European Space Agency (ESA), European Space Astronomy Centre (ESAC), Camino Bajo del Castillo s/n, 28692 Villanueva de la Cañada, Madrid, Spain
[19] School of Astronomy and Space Science, University of Chinese Academy of Sciences (UCAS), Beijing 100049, China
[20] National Astronomical Observatories, Chinese Academy of Sciences, Beijing 100101, China
[21] Institute for Frontiers in Astronomy and Astrophysics, Beijing Normal University, Beijing 102206, China
[22] Astrophysics Science Division, NASA Goddard Space Flight Center, 8800 Greenbelt Rd, Greenbelt, MD 20771, USA
[23] Department of Astronomy, The University of Texas at Austin, Austin, TX, USA
[24] Laboratory for Multiwavelength Astrophysics, School of Physics and Astronomy, Rochester Institute of Technology, 84 Lomb Memorial Drive, Rochester, NY 14623, USA
[25] George P. and Cynthia Woods Mitchell Institute for Fundamental Physics and Astronomy, Department of Physics and Astronomy, Texas A&M University, College Station, TX, USA
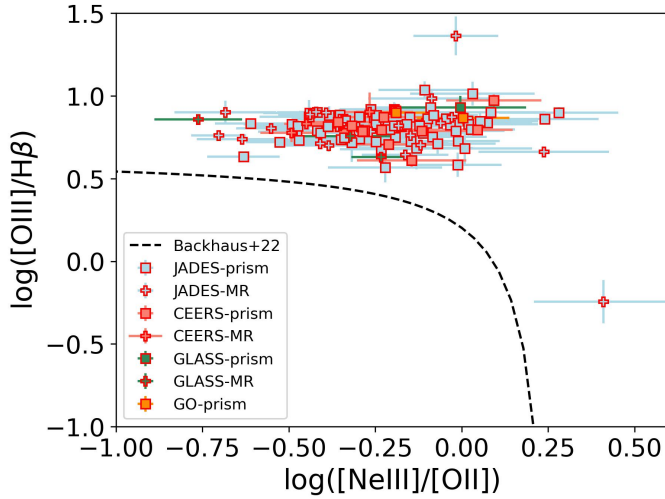[26] ESA/AURA Space Telescope Science Institute, Baltimore, USA

Fig. A.1. OHNO diagram for the galaxies in our sample. The symbols are the same as in Fig. 4. The dashed line indicates the demarcation line from Backhaus et al. (2022) to separate star-forming galaxies from AGNs. The AGN region lies above this line based on this diagnostic. Based on this diagnostic diagram, AGN candidates are shown as symbols with red edges.

Appendix A: Possible obscured AGNs

In Sect. 3.1 we removed unobscured AGNs with broad Balmer lines from our sample galaxies at $z = 4 - 10$. However, we note that our sample can still exhibit a contribution from obscured, narrow AGNs. To analyze this possible contamination, in this section we investigate the location of galaxies in some emission-line diagnostics. In particular, we analyze the OHNO diagram proposed in Backhaus et al. (2022) to separate the galaxies ionized by massive stars from those galaxies ionized by AGNs. We analyze the subsample of galaxies with detected [NeIII]λ3870 and the blended [OII]$\lambda\lambda$3726,3728 line. In Fig. A.1 we show the location of this subsample in the OHNO diagram. We note that all these galaxies are above the demarcation line and, therefore, could be AGNs. However, we remark that star-forming galaxies are also found in this locus, as seen in Fig. 6 in Backhaus et al. (2022). Therefore, it is not clear that this subsample is AGN-based only on this diagnostic diagram. For this reason, we analyze an alternative diagram that can be applied to this subsample. We choose the Mass-Excitation (MEx; Juneau et al. 2014) diagram, shown in Fig. A.2. Based on this diagnostic diagram, we note that most of the galaxies in our sample are star-forming galaxies. The subsample of AGN candidates based on the OHNO diagram is also in the locus of star-forming galaxies in the MEx diagram. Only a few candidates lie above the demarcation line from Juneau et al. (2014), but not above the one from Coil et al. (2015), at $z \sim 2.3$. We note, however, that the MeX diagram is not calibrated at the redshifts considered in this paper (Coil et al. 2015).

As a conclusion, based on these two diagnostics that are applicable to the galaxies in our sample, we cannot define a clear subsample of narrow AGNs. For this reason, we keep these sources in the final sample analyzed in this paper.

We explore whether there are biases in the relation we found in 4 due to the inclusion of these AGN candidates in our sample. In Fig. A.3, we show the location of the AGN candidates based on the OHNO diagram, in the relation between $\xi_{\rm ion}$ and redshift, indicated in Fig. 4. They show a wide range of redshifts from $z \sim 4 - 8$ and a wide range of $\xi_{\rm ion}$ values. They follow the trend
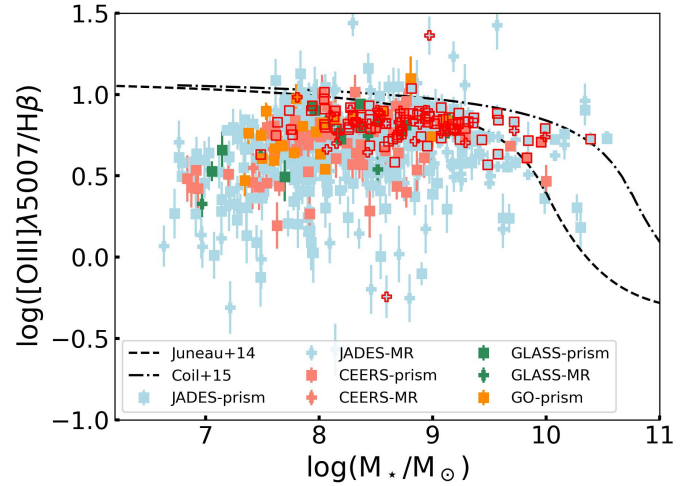

Fig. A.2. MEx diagram for the galaxies in our sample. The symbols are the same as in Fig. 4. The AGN candidates from Fig. A.1 are shown as symbols with red edges. The dashed black line indicates the demarcation between star-forming galaxies and AGNs, according to Juneau et al. (2014). The dashed-dotted black line is the demarcation at $z \sim 2$ (Coil et al. 2015).
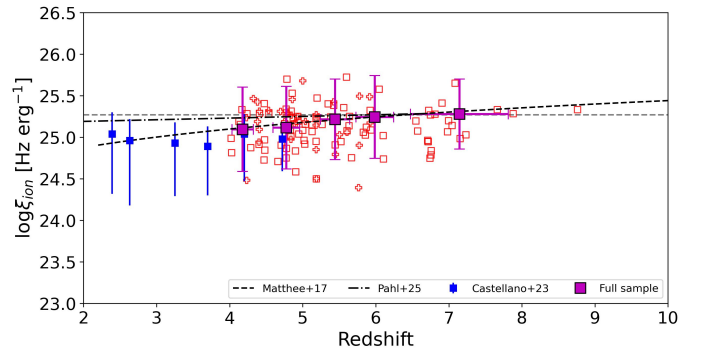

Fig. A.3. AGN candidates in the evolution of $\xi_{\rm ion}$ with redshift. The symbols are the same as in Fig. 4. The red symbols represent the AGN candidates from Fig. A.1.

of the median values of the full sample, which suggests there is no bias due to these candidates in the overall trend. Similar results are found if we analyze the relation of $\xi_{\rm ion}$ with the stellar mass, as shown in Fig. A.4. We show they have a wide range of stellar masses $\gtrsim 10^{7.5}\,{\rm M}_\odot$ and $\xi_{\rm ion}$ values. Similarly, they follow the trend that is observed with the median values of the full sample. Lastly, in Fig. A.5 we check the location of the AGN candidates in the relation of $\xi_{\rm ion}$ with M_{UV}. Similarly, we find that they show a wide range of M_{UV} and $\xi_{\rm ion}$ values. They are in general bright ($M_{UV} \lesssim -19$) compared to the full sample, which suggests this may be the reason [NeIII]λ3870 is detected in these candidates, rather than being ionized by AGNs. We also find that these candidates follow the trend observed with the median values of the full sample. Overall, we find that including these not secure AGN candidates in our sample does not affect the trends we find in this paper.

Appendix B: $\xi_{\rm ion}$ from Balmer lines

In Fig. B.1 we show a comparison between the values of $\xi_{\rm ion}$ determined from Hα and Hβ for the subsample of galaxies in the full sample with simultaneous detections of both Balmer lines.
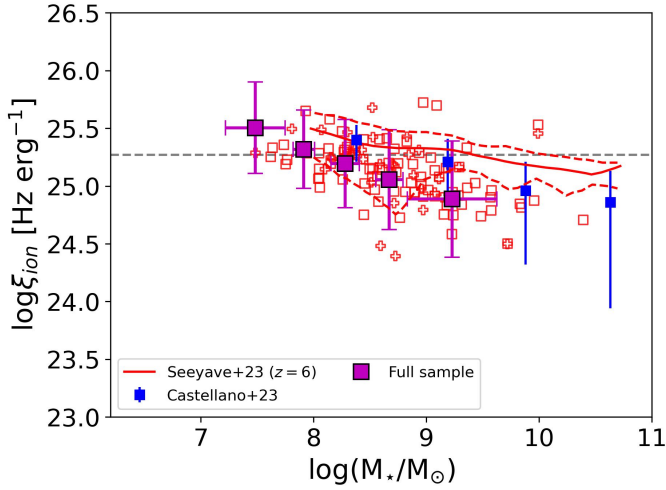
Fig. A.4. AGN candidates in the relation between $\xi_{\rm ion}$ and stellar mass. The symbols are the same as in Fig. 8. The red symbols represent the AGN candidates from Fig. A.1.
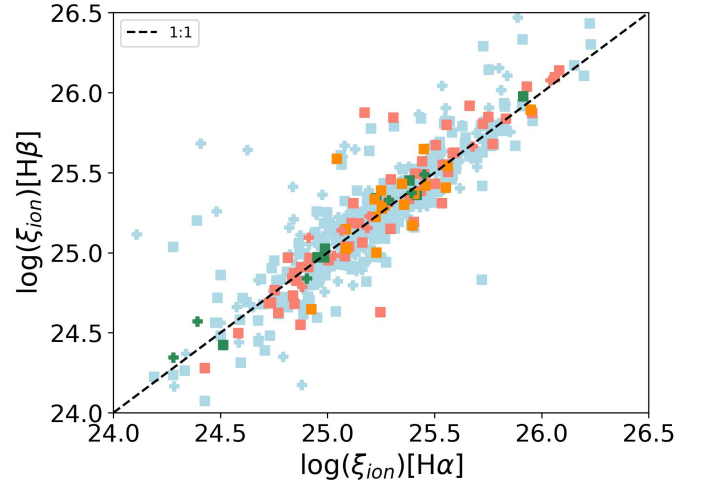

Fig. B.1. Comparison between $\xi_{\rm ion}$ determined from Hα and Hβ luminosities. The symbols represent individual galaxies in the sample with simultaneous detection of Hα and Hβ. The symbols are the same as in Fig. 4.
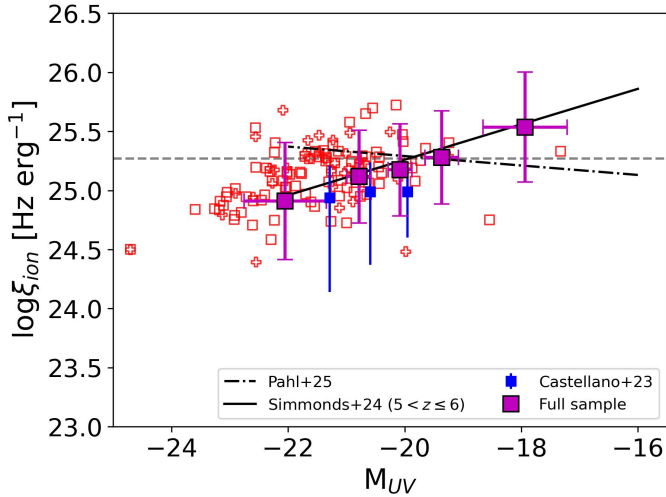
the distribution along the MS shown in Fig. 2. In our sample we do not include UV bright passive galaxies as seen in Fig. C.1. We also note that most of the galaxies in the complete subsample show $M_{UV} \lesssim -18$. We need to take into account these ranges in redshift and M_{UV} when analyzing the results since in these ranges we have a complete sample and the results are more robust.
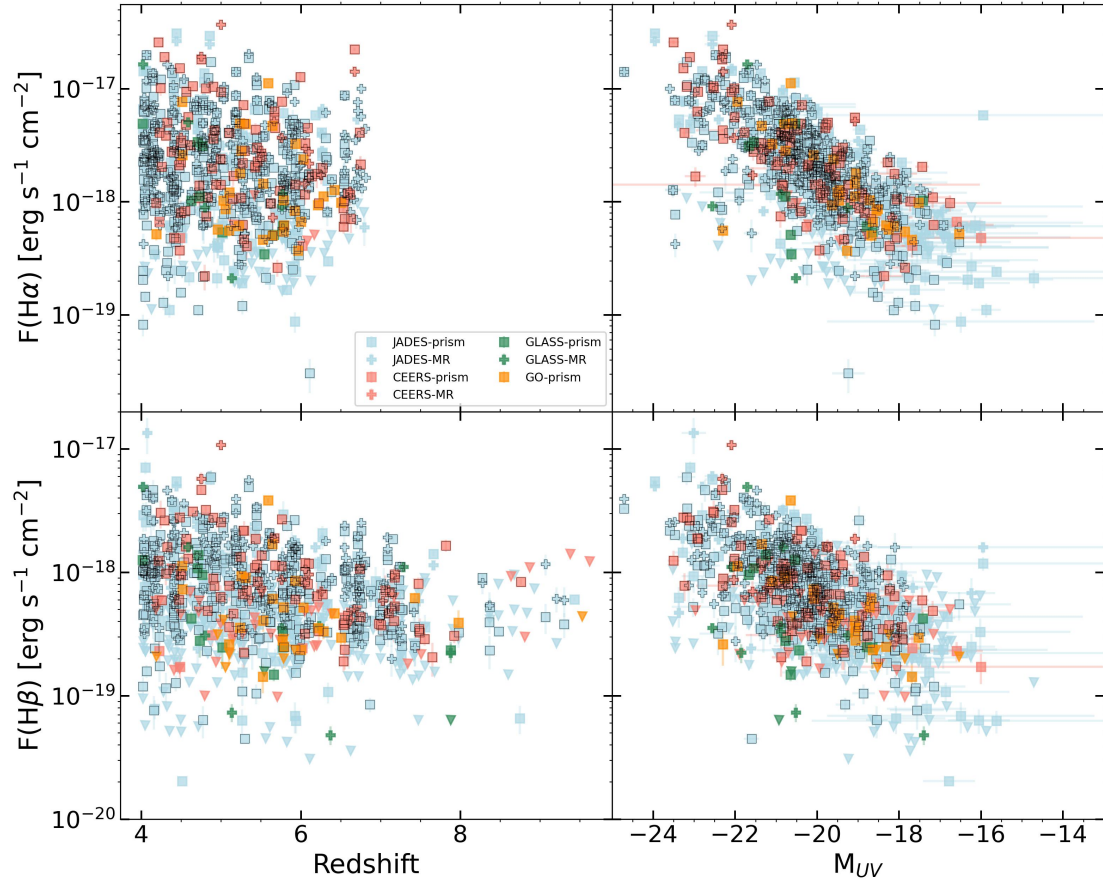

Fig. A.5. AGN candidates in the relation between $\xi_{\rm ion}$ and M_{UV}. The symbols are the same as in Fig. 5. The red symbols are the AGN candidates from Fig. A.1.

We find that there is good agreement between the two estimations with a median difference of 0.05 dex. Due to this fact, we do not introduce a bias when mixing both estimations in the galaxies where Hα is undetected.

Appendix C: Observed Balmer fluxes

In Fig. C.1 we show the relation between the observed fluxes of Balmer lines as a function of redshift and M_{UV}. We note that both Hα and Hβ cover a wide range of fluxes ($\sim$ 2dex). For Hα this distribution is uniform across all the redshifts ($z \lesssim 7$) while for Hβ we measured fluxes $< 2 \times 10^{-18}$ erg s^{-1} cm^{-2} for galaxies at $z \gtrsim 7$ and some of them are upper limits in flux. We also note that most of the complete subsample includes galaxies up to $z \sim 7$ for the two lines.

Regarding the relation between $\xi_{\rm ion}$ and M_{UV}, we find a decreasing trend in the fluxes with increasing M_{UV}, which indicates that the faintest UV galaxies show also fainter Balmer lines compared to brighter UV galaxies. This is in agreement with

Fig. C.1. Observed fluxes of Hα (top panels) and Hβ (bottom panels) as a function of redshift (left panels) and M$_{UV}$ (right panels). The symbols are the same as in Fig. 4.